Title

Nature and evolution of incommensurate charge order in manganites visualized with cryogenic scanning transmission electron microscopy

Journal

Proceedings of the National Academy of Sciences of the United States of America, 115(7)

ISSN

0027-8424

Authors

Baggari, Ismail El

Savitzky, Benjamin H

Admasu, Alemayehu S

et al.

Publication Date

2018-02-13

DOI

10.1073/pnas.1714901115

Peer reviewed

Nature and evolution of incommensurate charge order in manganites visualized with cryogenic scanning transmission electron microscopy

Ismail El Baggari[a], Benjamin H. Savitzky[a], Alemayehu S. Admasu[b,c], Jaewook Kim[b,c], Sang-Wook Cheong[b,c], Robert Hovden[d,1], and Lena F. Kourkoutis[d,e,2]

[a]Department of Physics, Cornell University, Ithaca, NY 14853; [b]Rutgers Center for Emergent Materials, Rutgers University, Piscataway, NJ 08854; [c]Department of Physics and Astronomy, Rutgers University, Piscataway, NJ 08854; [d]School of Applied and Engineering Physics, Cornell University, Ithaca, NY 14853; and [e]Kavli Institute for Nanoscale Science, Cornell University, Ithaca, NY 14853

Edited by Robert J. Cava, Princeton University, Princeton, NJ, and approved December 22, 2017 (received for review August 22, 2017)

Incommensurate charge order in hole-doped oxides is intertwined with exotic phenomena such as colossal magnetoresistance, high-temperature superconductivity, and electronic nematicity. Here, we map, at atomic resolution, the nature of incommensurate charge–lattice order in a manganite using scanning transmission electron microscopy at room temperature and cryogenic temperature (∼93 K). In diffraction, the ordering wave vector changes upon cooling, a behavior typically associated with incommensurate order. However, using real space measurements, we discover that the ordered state forms lattice-locked regions over a few wavelengths interspersed with phase defects and changing periodicity. The cations undergo picometer-scale (∼6 pm to 11 pm) transverse displacements, suggesting that charge–lattice coupling is strong. We further unearth phase inhomogeneity in the periodic lattice displacements at room temperature, and emergent phase coherence at 93 K. Such local phase variations govern the long-range correlations of the charge-ordered state and locally change the periodicity of the modulations, resulting in wave vector shifts in reciprocal space. These atomically resolved observations underscore the importance of lattice coupling and phase inhomogeneity, and provide a microscopic explanation for putative "incommensurate" order in hole-doped oxides.

charge order | incommensurate | manganite | electron microscopy | cryogenic STEM

Charge-ordered phases permeate the phase diagrams of strongly correlated systems such as cuprate high-temperature superconductors, colossal magnetoresistive manganites, and 2D transition-metal dichalcogenides (1–8). Charge order is a modulation of the electron density that breaks lattice translational symmetry and induces periodic lattice displacements (PLDs) via electron–lattice coupling. Bulk measurements have unearthed complex interactions between charge order and electronic phases, including direct competition with superconductivity or mediation of colossal magnetoresistance, which highlights the importance of charge order in understanding and manipulating novel phases of matter (2, 6–9).

While the precise microscopic mechanism of charge ordering remains under intense scrutiny, measurements of modulation wave vectors in various materials have established a tendency toward incommensurate order (1, 3, 5, 10–14). The presence of incommensuration coincides with the emergence of competing phases such as superconductivity and has motivated interrogation of the role of Fermi surface instabilities (10, 15–18). Scattering experiments, for instance, have measured changes in the positions of incommensurate wave vectors as a function of temperature, pressure, or doping, which is thought to reflect changes in the nesting of the Fermi surface. However, coupling to quenched impurities and attendant order parameter fluctuations profoundly alter correlation lengths and symmetry, and complicate experimental interpretation of reciprocal space behavior (14, 19, 20).

$Bi_{1-x}Sr_{x-y}Ca_yMnO_3$ (BSCMO) is a model charge-ordered manganite with a high, tunable transition temperature (T_c) (21, 22). Dark-field transmission electron microscopy has previously visualized striped superstructures in manganites, interpreting contrast as the ordering of holes on alternating manganese sites (Mn^{3+}–Mn^{4+}) (1, 3, 10). Other experiments based on transport and electron diffraction advance that charge order corresponds to a uniform charge density wave with small valence modulations (23, 24). The debate is partly motivated by the need to reconcile incommensurate wave vectors with discrete charge ordering. Understanding striped phases in manganites is further complicated by the ubiquity of quenched disorder and nanoscale phase inhomogeneity. Optical studies on BSCMO, for instance, suggest that long-range correlations gradually develop below T_c, an indication that charge order is disturbed by temperature-dependent spatial inhomogeneity (25). To achieve a microscopic understanding of charge-ordered states,

Significance

Charge order is a modulation of the electron density and is associated with unconventional phenomena, including colossal magnetoresistance and metal–insulator transitions. Determining how the lattice responds provides insights into the nature and symmetry of the ordered state. Scanning transmission electron microscopy can measure lattice displacements with picometer precision, but its use has been limited to room-temperature phases only. Here, we demonstrate high-resolution imaging at cryogenic temperature and map the nature and evolution of charge order in a manganite. We uncover picometer-scale displacive modulations whose periodicity is strongly locked to the lattice and visualize temperature-dependent phase inhomogeneity in the modulations. These results pave the way to understanding the underlying structure of charge-ordered states and other complex phenomena.

Author contributions: I.E.B. and L.F.K. designed research; I.E.B., B.H.S., A.S.A., J.K., S.-W.C., R.H., and L.F.K. performed research; I.E.B., B.H.S., R.H., and L.F.K. analyzed data; and I.E.B. and L.F.K. wrote the paper.

The authors declare no conflict of interest.

This article is a PNAS Direct Submission.

[1]Present address: Department of Materials Science and Engineering, University of Michigan, Ann Arbor, MI 48109.

[2]To whom correspondence should be addressed. Email: lena.f.kourkoutis@cornell.edu.

This article contains supporting information online at www.pnas.org/lookup/suppl/doi:10.1073/pnas.1714901115/-/DCSupplemental.

atomic-scale characterization of individual degrees of freedom is necessary.

Room-temperature scanning transmission electron microscopy (STEM) enables measurements of atomic column positions with picometer precision (26) and has been used to unravel, for instance, novel ferroelectric behavior in oxides (27, 28). Recently, we have revealed transverse, PLDs associated with charge ordering at room temperature in BSCMO ($T_c \approx 300$ K) and visualized nanoscale inhomogeneity in the modulation field (29). Here, we demonstrate cryogenic STEM imaging with sub-angstrom resolution (~0.78 Å) and sufficient signal-to-noise ratio to visualize the charge-ordered state in BSCMO well below T_c. Earlier cryogenic STEM studies have observed ordering phenomena (30, 31); however, stage instability, limited resolution, and low signal-to-noise ratio have precluded mapping of picometer-scale lattice behavior.

To understand the local structure of incommensurate modulations, we map picometer-scale lattice distortions associated with charge ordering near and well below T_c. At both temperatures, we find that the lattice modulations tend to form locally lattice-commensurate structures interspersed with regions of disorder and changing periodicity. By extracting the phase of the lattice modulations, we uncover nanoscale temperature-dependent phase variations which govern long-range ordering. The presence of phase slips and defects locally changes the periodicity of the modulations, resulting in a smaller wave vector at room temperature. Upon cooling, the phase field becomes more homogeneous, and the wave vector increases accordingly. The observations underscore the importance of lattice locking in a manganite, and provide a visualization of the real space structure of supposed incommensurate order. More generally, cryogenic STEM paves the way for direct visualization of correlated lattice order with picometer precision over atomic and nanometer scales.

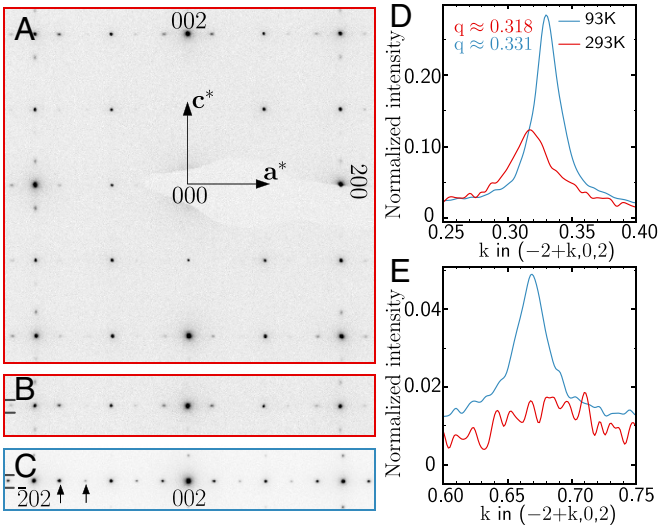

Fig. 1. Long-range order and wave vector variation upon cooling from 293 K to 93 K. (*A*) Typical electron diffraction pattern of BSCMO at 293 K. (*B* and *C*) Section of the diffraction pattern from $\bar{2}02$ to 202 at (*B*) 293 K and (*C*) 93 K. Arrows indicate superlattice peaks. (*D*) Projected intensity of the superlattice peak, *q*, near the $\bar{2}02$ Bragg peak along the **a*** direction. The intensity is integrated between the tick marks in *B* and *C* and is normalized by the $\bar{2}02$ Bragg peak intensity. Upon cooling, there is a change in the wave vector, from q = 0.318 r.l.u. at 293 K to q = 0.331 r.l.u. at 93 K, a behavior typically associated with incommensurate order. (*E*) Projected intensity near the 2*q* peak along the **a*** direction. The intensity is integrated between the tick marks in *B* and *C* and is normalized by the $\bar{2}02$ Bragg peak intensity. Colors are as in *D*.

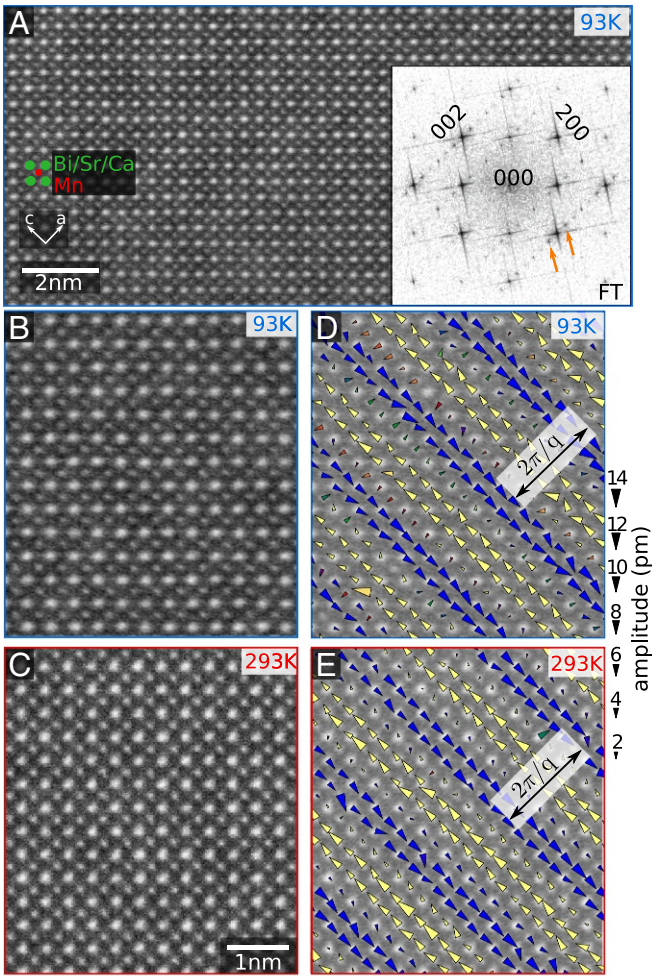

Fig. 2. Locally commensurate, picometer-scale PLDs at room and cryogenic temperatures. (*A*) HAADF STEM image and (*Inset*) its FT at 93 K. Bi/Sr/Ca columns (green) and Mn columns (red) are clearly resolved. The FT amplitude exhibits superlattice peaks (orange arrows) indicating the presence of a modulated structure. (*B* and *C*) HAADF STEM images at (*B*) 93 K and (*C*) 293 K. (*D* and *E*) Mapping of transverse, commensurate PLDs at (*D*) 93 K and (*E*) 293 K. Blue (yellow) arrows correspond to cation displacements oriented 90°(-90°) relative to **q**. Area of arrows scales linearly with the magnitude of displacements. *B*–*E* are the same scale as *C*.

Results

Wave Vector Shift in Diffraction. BSCMO single crystals are grown using the flux method, using Bi_2O_3, $CaCO_3$, $SrCO_3$, and Mn_2O_3, as reported previously (29). The Bi-based manganites display robust charge ordering ($T_c \approx$ 320 K to 525 K for $x = 0.5$) compared with their rare-earth counterparts ($RE_{1-x}Ca_xMnO_3$, RE = La, Nd, Pr) (21). We choose a doping level in which charge ordering is nascent at room temperature to study its structure near and well below T_c with cryogenic STEM. We measure the composition of BSCMO to be approximately $x = 0.65$ and $y = 0.47$ and find that a resistivity anomaly associated with charge ordering occurs at $T_c \approx$ 300 K (*SI Appendix*, Fig. S1). Previous reports on manganites have observed that the charge ordering wave vector, q, varies with doping, with $q \approx 1 - x$ reciprocal lattice units (r.l.u.) (3, 10); here, the doping level slightly deviates from $x = 2/3$ doping, and we expect incommensurate ordering.

Fig. 1*A* shows a typical, room-temperature (293 K) electron diffraction pattern of BSCMO, which we index in the *Pnma* space group. In addition to crystalline Bragg peaks, we observe

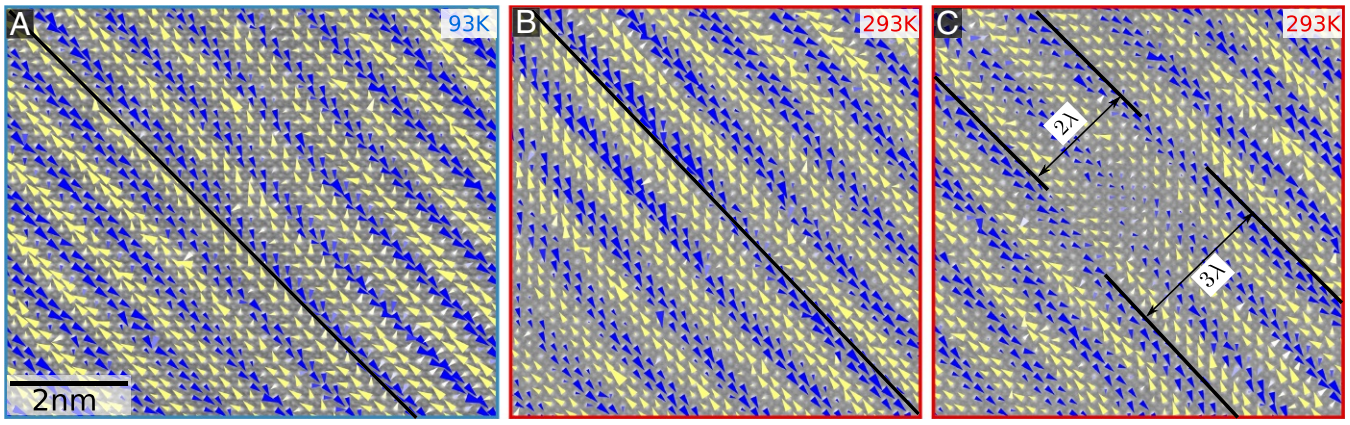

Fig. 3. Local variations and disorder of stripes. (*A* and *B*) Shear deformation of striped modulations at (*A*) 93 K and (*B*) 293 K. A shear deformation appears as a bending of the wavefronts. The black line traces the direction perpendicular to the wave vector and helps visualize the deformation of the wavefront. (*C*) Stripe dislocation at 293 K, in which one wavefront terminates abruptly. The modulation wavelength is $\lambda = 2\pi/q$. *B* and *C* are the same scale as *A*.

superlattice peaks at $\pm\mathbf{q}$ indicating the presence of a periodic modulation at both 293 K (Fig. 1*B*) and 93 K (Fig. 1*C*). The projected intensity of the $(-2+q,0,2)$ peak along $\mathbf{a}^*$ at 293 K (red) and 93 K (blue) is shown in Fig. 1*D*. At each temperature, the intensity profile is obtained by integrating between the tick marks in Fig. 1 *B* and *C*, and is normalized by the respective integrated intensity of the $\bar{2}02$ Bragg peak. We note a clear shift in the superlattice peak position upon cooling, from $q = 0.318$ r.l.u. at 293 K to $q = 0.331$ r.l.u. at 93 K (*SI Appendix*, Fig. S15). By fitting multiple satellites in the diffraction pattern, we obtain the average wave vector and its uncertainty at each temperature. The average wave vector is $q = 0.314 \pm 0.003$ r.l.u. at 293 K and $q = 0.332 \pm 0.001$ r.l.u. at 93 K. The magnitude of the wave vector shift is $\delta q = 0.018 \pm 0.003$ r.l.u. Temperature-dependent wave vector variations, as observed here, are typically considered an indication of incommensurate order.

In addition to a shift in the wave vector, the superlattice peak exhibits a clear increase in intensity, I, and a decrease in the full-width-at-half maximum, σ_k, at low temperature. Fitting a Lorentzian function and a linear background to the projected q peak, we find that $I(93\text{K})/I(293\text{K}) \approx 1.46$ and $\sigma_k(93\text{ K})/\sigma_k(293\text{ K}) \approx 0.57$ (*SI Appendix*, Fig. S15). The weaker $2q$ peak, while almost undetectable at room temperature, is relatively sharp and well defined at 93 K (Fig. 1*E*). These observations indicate that charge order strength and correlations increase well below T_c.

Real Space Imaging of Lattice Order. From previous real space measurements at room temperature, we uncovered PLDs associated with charge ordering in BSCMO (29). PLDs, $\Delta(\mathbf{r})$, may be described by the order parameter

$$\Delta(\mathbf{r}) = \Re\mathfrak{e}\{\mathbf{A}(\mathbf{r})e^{i\phi(\mathbf{r})}e^{\mathbf{iq}.\mathbf{r}}\},$$

where $\mathbf{A}(\mathbf{r})$ is the displacement vector, $\mathbf{q}$ is the wave vector, and $\phi(\mathbf{r})$ is the phase. The modulations give rise to complex-valued satellite peaks in the Fourier transform (FT) which are given by $S(\mathbf{k}) \sim \sum_{\{\mathbf{r}\}} \exp[i(\mathbf{k} \pm \mathbf{q}).\mathbf{r}] \exp[i\phi(\mathbf{r})]$, where $\{\mathbf{r}\}$ is the set of lattice positions (*SI Appendix*, *Structure Factor of Periodic Lattice Displacements*). Phase information encodes not only the particular realization of $\Delta(\mathbf{r})$ but also its disorder. Since diffraction experiments probe the intensity ($I(\mathbf{k}) \approx |S(\mathbf{k})|^2$), they are insensitive to phase information and provide, instead, globally averaged measurements of correlation lengths, intensities, and wave vectors (6). However, the microscopic picture of incommensurate modulations and their temperature (or doping) dependence may be linked to phase information (14).

To overcome challenges associated with intensity-based techniques, we characterize $\Delta(\mathbf{r})$ using phase-sensitive, real space STEM. Fig. 2*A* shows a high-angle annular dark-field (HAADF) STEM lattice image at 93 K; Bi/Sr/Ca columns (green) appear bright, Mn columns (red) appear faint, and O atoms are invisible. The contrast is due to the dependence of the scattering cross-section in HAADF STEM on the atomic number. The temperature of the sample (~93 K) is directly read from a thermocouple near the tip of the sample rod, but the true temperature may be slightly higher. To minimize stage drift and noise, stacks of 40 fast-acquisition (0.5 μs per pixel) images are collected, registered by cross-correlation, and averaged. The data demonstrate STEM imaging near liquid nitrogen temperature (~93 K) with high resolution (~0.78 Å) and signal-to-noise ratio (*SI Appendix*,

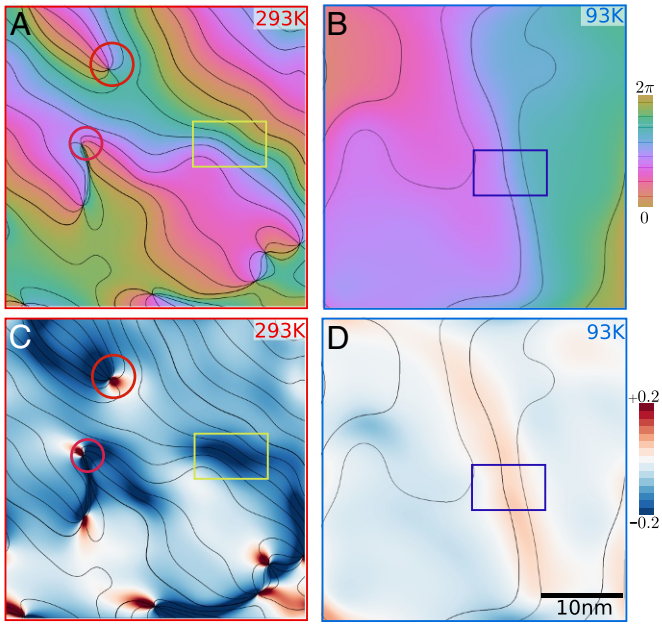

Fig. 4. Emergent phase coherence at low temperature. (*A* and *B*) Maps of the coarse-grained phase, $\phi(\mathbf{r})$, at (*A*) 293 K and (*B*) 93 K. Black lines represent constant $\pi/4$ phase contours. (*C* and *D*) Maps of the phase strain, ε_c, at (*C*) 293 K and (*D*) 93 K. Circles correspond to dislocations, and boxes correspond to shear deformations. *A*–*C* are the same scale as *D*.

Fig. S2), which may be combined with picometer precision mapping of atomic columns.

The FT (Fig. 2*A*, *Inset*) of the lattice image exhibits sharp superlattice spots (arrows), allowing mapping of lattice modulations associated with superlattice peaks (29). We damp the amplitude of the superlattice peaks to the background level and apply an inverse FT. The result is a reference lattice image in which the targeted modulation has been removed (*SI Appendix*, Fig. S3). By fitting atomic columns using 2D Gaussian functions in both the original lattice and the reference lattice, we may obtain lattice shifts associated with the charge-ordered state. As previously discussed, the method accurately yields the structure of the modulation except at atomically sharp discontinuities in the modulation field (29).

Fig. 2 *B* and *D* shows a STEM image at 93 K and the corresponding mapping of the lattice response, respectively. The arrows correspond to displacements of atomic columns in the original image relative to the generated reference lattice, and the color represents the angle of the displacement vector relative to **q**, with blue (yellow) corresponding to 90° (-90°). Thus, the low-temperature ordered state in BSCMO involves transverse, displacive modulations of both the Bi/Sr/Ca sites and the Mn sites, with amplitudes in the range of 6 pm to 11 pm. For comparison, Fig. 2 *C* and *E* shows a STEM image and the corresponding PLD mapping at 293 K. The displacements appear to stack coherently along the b direction, since we do not observe intensity variations between modulated and unmodulated Mn sites (*SI Appendix*, Fig. S4). Due to electron channeling effects, such intensity variations are expected if the displacements stack incoherently (32). By imaging other zone axes of the crystal (*SI Appendix*, Figs. S4–S6), we do not observe out-of-plane displacements or modulations, which suggests that the PLDs in BSCMO occur primarily in the ac plane. These observations are consistent with neutron and X-ray powder refinements on related manganite systems, where bond length variations are observed along the modulation wave vector only (33, 34). At both temperatures, the lattice displacements are visually lattice-commensurate with three-unit cell periodicity, but only over four to five PLD wavelengths.

Phase and Periodicity Variations. As shown in *Wave Vector Shift in Diffraction*, area-averaged diffraction yields an incommensurate wave vector at 293 K and an (almost) commensurate wave vector at 93 K. To understand the nature of incommensurate order, it is important to determine whether the periodicity from diffraction data reflects a long-range incommensurate state with uniform periodicity or some other local structures. To that end, we measure q from the FT amplitude of multiple STEM datasets with fields of view ranging from 17 nm to 40 nm. The wave vectors from local measurements span a wide range of values (*SI Appendix*, *Phase Variations and Wavevector Shifts* and Fig. S8). At room temperature, they range from $q = 0.307$ r.l.u. to $q = 0.331$ r.l.u. and are generally smaller than the commensurate value of $q = 1/3$ r.l.u. Interestingly, the PLD even appears lattice-commensurate up to seven wavelengths in a well-ordered region at room temperature, with $q = 0.331$ r.l.u. (*SI Appendix*, *Phase Variations and Wavevector Shifts* and Figs. S11 and S12). At 93 K, the wave vectors range from $q = 0.329$ r.l.u. to $q = 0.340$ r.l.u. and are generally larger than $q = 1/3$ r.l.u. The wave vector remains smaller than the predicted value from the empirical relation $q \approx 1 - x \approx 0.35$ r.l.u., which suggests that the wave vector may continue to increase upon further cooling. These observations expose a discrepancy between local (tens on nanometers) and global (micron scale) measurements of the modulation wave vector, and suggest that incommensuration reflects spatially complex textures and periodicities.

Bridging the gap in length scales, we map PLDs over larger areas and show that they undergo spatial variations in their shape and strength (Fig. 3). In particular, we observe intrinsic stripe defects, including shear deformations, dislocations, and amplitude reduction. A shear deformation is a bending of a wavefront, as shown in Fig. 3 *A* and *B*. Both the 293 K map and the 93 K map reveal such deformation, with the latter exhibiting a milder and more extended instance. We also observe other forms of disorder in 293 K data, including stripe dislocations where a wavefront terminates abruptly (Fig. 3*C*). Displacement magnitudes reduce near defect sites, with dislocations showing a more pronounced reduction. Over a few wavelengths, we observe the lattice-locked structures shown in Fig. 2. However, we also observe locally varying periodicities, particularly near defects, reflecting the compression of wavefronts (Fig. 3 and *SI Appendix*, Fig. S9).

Analysis of the demodulated order parameter, $A(\mathbf{r})^{i\phi(\mathbf{r})}$, unearths nanoscale phase inhomogeneity that coincides with the deformations and dislocations of stripes. Phase variations encode deviations from perfect, long-range modulations; they can be extracted using the phase lock-in technique applied previously on spectroscopic scanning tunneling microscopy data to visualize density wave fluctuations in cuprates (13, 35) (*SI Appendix*, *Extracting Coarse-Grained Order Parameter Fields*). Fig. 4*A* displays a room-temperature phase configuration, $\phi(\mathbf{r})$, overlaid with $\pi/4$ constant phase contours (black lines). The $\phi(\mathbf{r})$ map reveals significant spatial inhomogeneity, with $\pm\pi$ phase changes, or more than four contours, occurring within regions as small as 5 nm. Even more dramatic variations occur near topological defects (dislocations) where the phase winds by $\pm 2\pi$ around the defect site (circles). In contrast, we observe, in Fig. 4*B*, a more uniform, slowly varying phase configuration at 93 K with a dearth of $\pm 2\pi$ phase change over tens of nanometers.

Phase variations are better visualized via the compressive phase strain, $\varepsilon_c = \mathbf{q}/q \cdot \nabla\phi(\mathbf{r})$ (36). Phase strain is normalized such that a $\pm 2\pi$ phase shift over one wavelength ($\lambda = 2\pi/q$) corresponds to ± 1, and a positive (negative) phase strain represents a local compression (expansion) of the wavefronts (*SI Appendix*, Figs. S9–S11, S13, and S14). In Fig. 4 *C* and *D*, we show ε_c maps overlaid with phase contours at 293 K and 93 K, respectively. We observe, at room temperature, a moderate background strain, punctured by regions of large, localized phase gradients, notably near dislocations (circle) and shear deformations (rectangle). The ε_c map at 93 K exhibits mild variations and much smaller strain values throughout the full

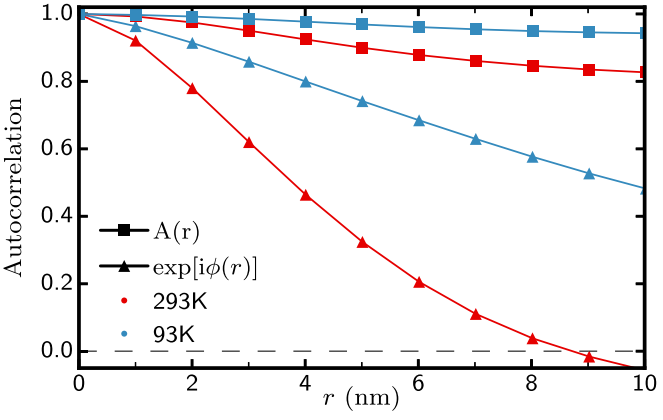

Fig. 5. Autocorrelations of the phase component and the amplitude component at 293 K (red) and 93 K (blue). Lines are guides for the eye. The slow decay of amplitude correlations at both temperatures suggests that the amplitude is not the main driver of long-range order. In contrast, the strong temperature-dependent decay of phase correlations supports that phase variations govern long-range order.

field of view, an indication of emergent phase homogeneity well below T_c.

Gradients in the phase result in superlattice peak shifts in the FT amplitude, assuming variations do not average to zero (*SI Appendix*, *Phase Variations and Wavevector Shifts* and Figs. S9–S11, S13, and S14). The shift is given by $\delta\mathbf{q} = \mathbf{q} - \mathbf{q_0} = \langle\nabla\phi(\mathbf{r})\rangle$, where $\mathbf{q_0}$ is the wave vector in the absence of phase variation. At room temperature, large negative phase strain results in the reduction of q, as measured in diffraction or STEM FT amplitudes. Upon cooling, the compressive phase strain increases, and, consequently, the wave vector increases. The PLD mappings suggest that the modulations are often lattice-commensurate over a few wavelengths, and that, absent phase variations, we obtain $q \approx 1/3$ r.l.u. (Fig. 2 and *SI Appendix*, *Phase Variations and Wavevector Shifts* and Figs. S9–S12). In this picture, charge–lattice order favors lattice-locked structures, and the changes in incommensurate wave vectors reflect deformations of the phase field.

In regions where the PLD appears lattice-locked, the modulation may instead be incommensurate with a very large periodicity given by $1/\delta q$. Due to the limited fields of view in imaging, we cannot completely distinguish such incommensurate structure from a commensurate structure with local phase slips, especially when the incommensuration is small. However, the intertwined spatial variations of the phase and the wave vectors, as observed in our data, disfavor a long-range incommensurate state with a uniform periodicity (*SI Appendix*, *Phase Variations and Wavevector Shifts* and Figs. S9–S12). We reiterate that, due to phase variations, amplitude-based probes detect shifts in incommensurate wave vectors, which are consistent with several distinct local structures. On the other hand, phase-sensitive probes, including STEM, can measure the distribution of periodicities and textures of ordered states at the atomic scale.

Phase and Amplitude Disorder. Having revealed temperature-dependent phase disorder, we address the relative weights of amplitude and phase variations by calculating their respective autocorrelations. In Fig. 5, we observe that amplitude correlations quickly plateau to ~ 0.9 at 293 K and ~ 0.8 at 93 K over accessible length scales (~ 10 nm for reasonable statistics); their slow decay at both temperatures suggests they do not influence the correlation length of stripes. Phase correlations, on the other hand, decay rapidly at 293 K, becoming completely uncorrelated beyond ~ 8 nm. At 93 K, they remain finite and relatively significant (~ 0.5) beyond 10 nm. The strong temperature dependence of phase correlations suggests that the phase component is the primary driver of long-range order. The situation invites an analogy to disordered superconductors where the loss of phase coherence can cause a superconductor-to-insulator transition despite the persistence of a finite amplitude (37).

Finally, local inspection of amplitude fields at 293 K and 93 K (*SI Appendix*, Fig. S7) reveals an interaction between phase variation and amplitude variation. From a mean field perspective, amplitude fluctuations should be suppressed because they cost finite energy. When the phase varies slowly, the amplitude is expectedly robust and uniform. However, in regions of large phase gradients, the amplitude weakens, particularly at dislocation sites where it collapses completely (*SI Appendix*, *Phase Variation and Amplitude Variation* and Fig. S7). Phase deformations increase the elastic energy density by an amount proportional to $|\nabla\phi(\mathbf{r})|^2$, which may require amplitude suppression in regions of diverging phase gradients (38, 39). Our observations are consistent with this picture, and attest to the importance of phase fluctuations in shaping the strength and correlations of charge order.

Discussion

Based on these results, we propose that experimental observations of coincident incommensuration and emergent competing states are related to the local disordering of the phase component; phase gradients account for (*i*) the reduction of the correlation length, (*ii*) changes in the average wave vector, and (*iii*) the local quenching of the amplitude which may allow another order to materialize. This may explain the competition between ferromagnetism and incommensurate charge order in manganites (1, 10), or even the granular interplay between short-range incommensurate charge density waves and superconductivity in cuprates or transition metal dichalcogenides.

A successful microscopic theory for charge order, and the many exotic states it affects, should account for all relevant degrees of freedom and for the possibility of inhomogeneity. Using cryogenic STEM on a manganite, we have directly measured the lattice component and found that the cations undergo transverse displacements relative to the modulation wave vector. Models based solely on separation of charge or orbital ordering are therefore insufficient. Atomic displacements change bond distances, bond angles, and hence exchange interactions, and may be key to explaining how charge order impacts other electronic states. We have also visualized the interplay between incommensuration, phase defects, and lattice locking, reinforcing both the importance of charge–lattice coupling and the fundamental effects of nanoscale phase inhomogeneity on macroscopic behavior. We envision that mapping the lattice component using cryogenic STEM in correlated materials will elucidate structural ground states and reveal connections between atomic displacements and various symmetries of electronic and orbital order.

Materials and Methods

Sample Preparation. BSCMO single crystals are grown using the flux method, using Bi_2O_3, $CaCO_3$, $SrCO_3$, and Mn_2O_3 (29). Sample preparation for electron microscopy and energy dispersive X-ray spectroscopy (EDX) are performed on an FEI Strata 400 Focused Ion Beam. From EDX, the composition is determined to be approximately $x = 0.65$ and $y = 0.47$, with negligible variations over the whole sample (size 0.34 × 0.28 mm).

Electron Diffraction and STEM. We perform electron diffraction and microscopy on an aberration-corrected FEI Titan Themis operating at 300 kV. Diffraction measurements across temperatures are performed in the same region of the sample using a ~1-μm selected area aperture. In HAADF-STEM, the convergence semiangle is 30 mrad, and the collection inner and outer angles are 68 and 340 mrad, respectively. For cryogenic experiments, we use a Gatan 636 double-tilt liquid nitrogen holder. Due to reduced stability at cryogenic temperatures, stacks of 20 to 40 fast-acquisition (0.5 μs per pixel dwell time) images are collected, registered by cross-correlation, and averaged to minimize stage drift and noise.

ACKNOWLEDGMENTS. Research was primarily supported by the Department of Defense, Air Force Office of Scientific Research under Award FA 9550-16-1-0305. We also acknowledge support by the Packard Foundation. This work made use of the Cornell Center for Materials Research Shared Facilities, which are supported through the National Science Foundation (NSF) Materials Research Science and Engineering Centers (MRSEC) program (DMR-1719875). The FEI Titan Themis 300 was acquired through Grant NSF-MRI-1429155, with additional support from Cornell University, the Weill Institute, and the Kavli Institute at Cornell. B.H.S. was supported by NSF Graduate Research Fellowship Program (GRFP) Grant DGE-1144153. The work at Rutgers was supported by the Gordon and Betty Moore Foundation's Emergent Phenomena in Quantum Systems (EPiQS) Initiative through Grant GBMF4413 to the Rutgers Center for Emergent Materials.

1. Chen C, Cheong SW (1996) Commensurate to incommensurate charge ordering and its real-space images in $La_{0.5}Ca_{0.5}MnO_3$. *Phys Rev Lett* 76:4042–4045.
2. Uehara M, Mori S, Chen CH, Cheong SW (1999) Percolative phase separation underlies colossal magnetoresistance in mixed-valent manganites. *Nature* 399:560–563.
3. Chen CH, Mori S, Cheong SW (1999) Anomalous melting transition of the charge-ordered state in manganites. *Phys Rev Lett* 83:4792–4795.
4. Wu T, et al. (2011) Magnetic-field-induced charge-stripe order in the high-temperature superconductor $YBa_2Cu_3O_y$. *Nature* 477:191–194.

5. Ghiringhelli G, et al. (2012) Long-range incommensurate charge fluctuations in (Y,Nd)$Ba_2Cu_3O_{6+x}$. *Science* 337:821–825.
6. Chang J, et al. (2012) Direct observation of competition between superconductivity and charge density wave order in $YBa_2Cu_3O_{6.67}$. *Nat Phys* 8:871–876.
7. Kusmartseva AF, Sipos B, Berger H, Forro L, Tutiš E (2009) Pressure induced superconductivity in pristine 1 T- $TiSe_2$. *Phys Rev Lett* 103:236401.
8. Li LJ, et al. (2016) Controlling many-body states by the electric-field effect in a two-dimensional material. *Nature* 529:185–189.
9. Zhang J, et al. (2016) Cooperative photoinduced metastable phase control in strained manganite films. *Nat Mater* 15:956–960.
10. Milward GC, Calderón MJ, Littlewood PB (2005) Electronically soft phases in manganites. *Nature* 433:607–610.
11. Feng Y, et al. (2015) Itinerant density wave instabilities at classical and quantum critical points. *Nat Phys* 11:865–871.
12. Comin R, Damascelli A (2016) Resonant X-ray scattering studies of charge order in cuprates. *Annu Rev Condens Matter Phys* 7:369–405.
13. Mesaros A, et al. (2011) Topological defects coupling smectic modulations to intra-unit-cell nematicity in cuprates. *Science* 333:426–430.
14. Mesaros A, et al. (2016) Commensurate $4a_0$-period charge density modulations throughout the $Bi_2Sr_2CaCu_2O_{8+x}$ pseudogap regime. *Proc Natl Acad Sci USA* 113:12661–12666.
15. Chuang YD, Gromko A, Dessau D, Kimura T, Tokura Y (2001) Fermi surface nesting and nanoscale fluctuating charge/orbital ordering in colossal magnetoresistive oxides. *Science* 292:1509–1513.
16. Morosan E, et al. (2006) Superconductivity in Cu_xTiSe_2. *Nat Phys* 2:544–550.
17. Sipos B, et al. (2008) From Mott state to superconductivity in 1T-TaS_2. *Nat Mater* 7:960–965.
18. Wise WD, et al. (2008) Charge-density-wave origin of cuprate checkerboard visualized by scanning tunnelling microscopy. *Nat Phys* 4:696–699.
19. Kivelson SA, et al. (2003) How to detect fluctuating stripes in the high-temperature superconductors. *Rev Mod Phys* 75:1201–1241.
20. Del Maestro A, Rosenow B, Sachdev S (2006) From stripe to checkerboard ordering of charge-density waves on the square lattice in the presence of quenched disorder. *Phys Rev B Condens Matter Mater Phys* 74:1–10.
21. Frontera C, et al. (2002) Anomalously high charge/orbital ordering temperature in $Bi_{0.5}Sr_{0.5}MnO_3$. *Appl Phys A* 74:s1787–s1789.
22. Kim BH, et al. (2007) Evidence of the Bi(3+) lone-pair effect on the charge-ordering state: Resistivity and thermoelectric power of $Bi_{0.5-y}La_ySr_{0.5}MnO_3$ ($0.0 \leq y \leq 0.4$). *J Phys Condens Matter* 19:296205.
23. Loudon JC, et al. (2005) Weak charge-lattice coupling requires reinterpretation of stripes of charge order in $La_{1-x}Ca_xMnO_3$. *Phys Rev Lett* 94:5–8.
24. Cox S, Singleton J, McDonald RD, Migliori A, Littlewood PB (2008) Sliding charge-density wave in manganites. *Nat Mater* 7:25–30.
25. Rübhausen M, Yoon S, Cooper SL, Kim KH, Cheong SW (2000) Anisotropic optical signatures of orbital and charge ordering in $Bi_{1-x}Ca_xMnO_3$. *Phys Rev B* 62:R4782–R4785.
26. Yankovich AB, et al. (2014) Picometre-precision analysis of scanning transmission electron microscopy images of platinum nanocatalysts. *Nat Commun* 5: 4155.
27. Nelson CT, et al. (2011) Spontaneous vortex nanodomain arrays at ferroelectric heterointerfaces. *Nano Lett* 11:828–834.
28. Zhang Q, et al. (2013) Direct observation of multiferroic vortex domains in $YMnO_3$. *Sci Rep*, 3:2741.
29. Savitzky BH, et al. (2017) Bending and breaking of stripes in a charge ordered manganite. *Nat Commun* 8:1883.
30. Klie RF, et al. (2007) Direct measurement of the low-temperature spin-state transition in $LaCoO_3$. *Phys Rev Lett* 99:1–4.
31. Hovden R, et al. (2016) Atomic lattice disorder in charge-density-wave phases of exfoliated dichalcogenides (1T-TaS_2). *Proc Natl Acad Sci USA* 113:11420–11424.
32. Haruta M, Kurata H, Komatsu H, Shimakawa Y, Isoda S (2009) Effects of electron channeling in HAADF-STEM intensity in La_2CuSnO_6. *Ultramicroscopy* 109:361–367.
33. Goff R, Attfield J (2004) Charge ordering in half-doped manganites. *Phys Rev B* 70:140404.
34. Fernandez-Diaz M, Martinez J, Alonso J, Herrero E (1999) Structural, thermal, transport, and magnetic properties of the charge-ordered $La_{1/3}Ca_{2/3}MnO_3$ oxide. *Phys Rev B* 59:1277–1284.
35. Lawler MJ, et al. (2010) Intra-unit-cell electronic nematicity of the high-T_c copper-oxide pseudogap states. *Nature* 466:347–351.
36. Feinberg D, Friedel J (1988) Elastic and plastic deformations of charge density waves. *J Phys* 49:485–496.
37. Emery VJ, Kivelson SA (1995) Importance of phase fluctuations in superconductors with small superfluid density. *Nature* 374:434–437.
38. Hall RP, Hundley MF, Zettl A (1988) Switching and charge-density-wave transport in $NbSe_3$. I. DC characteristics. *Phys Rev B* 38:13002–13018.
39. Coppersmith SN, Millis AJ (1991) Diverging strains in the phase-deformation model of sliding charge-density waves. *Phys Rev B* 44:7799–7807.